Icarus 142, 536–549 (1999)
Article ID icar.1999.6216, available online at http://www.idealibrary.com on IDEAL®

Near-Infrared Spectra of Icy Outer Solar System Surfaces: Remote Determination of H_2O Ice Temperatures

W. M. Grundy, M. W. Buie, J. A. Stansberry,[1] and J. R. Spencer

Lowell Observatory, 1400 West Mars Hill Road, Flagstaff, Arizona 86001
E-mail: grundy@lowell.edu

and

B. Schmitt[2]

CNRS/LGGE, 54 rue Molière, BP 96 Domaine Universitaire, 38402 St-Martin-d'Hères, France

Received January 6, 1999; revised August 10, 1999

We present new 1.20 to 2.35 μm spectra of satellites of Jupiter, Saturn, and Uranus, and the rings of Saturn, obtained in 1995 and 1998 at Lowell Observatory. For most of the target objects, our data provide considerable improvement in spectral resolution and signal-to-noise over previously published data. Absorption bands with shapes characteristic of low-temperature, hexagonal crystalline H_2O ice dominate the spectra of most of our targets in this wavelength range. We make use of newly published temperature-dependent wavelengths and relative strengths of H_2O absorption bands to infer ice temperatures from our spectra. These ice temperatures are distinct from temperatures determined from thermal emission measurements or simulations of radiative balances. Unlike those methods, which average over all terrains including ice-free regions, our temperature-sensing method is only sensitive to the ice component. Our method offers a new constraint which, combined with other observations, can lead to better understanding of thermal properties and textures of remote, icy surfaces. Ice temperatures are generally lower than thermal emission brightness temperatures, indicative of the effects of thermal inertia and segregation between ice and warmer, darker materials. We also present the results of experiments to investigate possible changes of water ice temperature over time, including observations of Titania at two epochs, and of Ganymede and saturnian ring particles following emergence from the eclipse shadows of their primary planets. Finally, we discuss limitations of our temperature measurement method which can result from the presence of H_2O in phases other than hexagonal ice-I_h, such as amorphous ice, hydrated mineral phases, or radiation-damaged crystalline ice. Our spectra of Europa and Enceladus exhibit peculiar spectral features which may result from effects such as these.

© 1999 Academic Press

Key Words: **ices; spectroscopy; surfaces, satellite; infrared observations.**

INTRODUCTION

As it became technically feasible to obtain near-infrared spectra of the satellites and rings of outer Solar System planets, it was recognized that strong water-ice absorptions at 1.5, 2, and 3 μm dominated the near-infrared albedo spectra of many of these objects (e.g., Kuiper *et al.* 1970, Pilcher *et al.* 1970, 1972, Fink *et al.* 1973, 1976, Morrison *et al.* 1976, Cruikshank 1980, Cruikshank and Brown 1981, and Soifer *et al.* 1981). Ockman (1958) noted variations with temperature in the near-infrared absorption coefficient spectrum of H_2O ice, particularly an absorption band at 1.65 μm which becomes progressively stronger as the ice temperature is reduced. The possibility of using this band to determine surface temperatures of icy satellites was immediately recognized, following the identification of H_2O ice absorptions in spectra of outer Solar System objects (e.g., Kieffer and Smythe 1974). Fink and Larson (1975) proposed an easily calculable index consisting of the ratio between the equivalent widths of the narrow absorption band at 1.65 μm and of the broader band-complex ranging from 1.4 to 1.8 μm. The temperature calibration curve for this ratio was based on laboratory frost spectra, rather than direct measurements of optical constants and simulation of radiative transfer in a particulate surface. Clark (1981) pointed out that differences in texture between laboratory frosts and the surfaces of actual Solar System objects could result in errors in temperatures derived from the Fink and Larson band-area ratio. Clark (1981) also asserted that there was no evidence of any temperature-dependent wavelength shifts in the water ice bands and that the 1.65 μm band was "poorly suited to temperature sensing" because, like all absorption bands, the band shape and depth depend on surface texture. This pessimism,

[1] Current address: Steward Observatory, University of Arizona, 933 N. Cherry Ave., Tucson, AZ 85721-0065.

[2] Current address: Laboratoire de Planetologie de Grenoble, Batiment D de Physique, B.P. 53, 38041 Grenoble Cedex 9, France.

0019-1035/99 $30.00
Copyright © 1999 by Academic Press
All rights of reproduction in any form reserved.

compounded by the difficulty of simulating infrared spectral reflectance of icy, granular surfaces prior to the introduction of Hapke theory (e.g., Hapke 1981, 1993) and the paucity of published absorption coefficients of low temperature ice, resulted in little subsequent use being made of the temperature-dependence of the near-infrared water ice absorption bands.

Recently, measurements of temperature-dependent near-infrared absorption coefficients of H_2O ice were published by Grundy and Schmitt (1998). They showed quantitatively how, as ice temperature decreases, the 1.5, 1.65, and 2 μm absorptions all shift to longer wavelengths, while components at 1.31 and 1.65 μm increase in strength, and the shapes of other bands and continuum regions change subtly. Grundy and Schmitt proposed that this suite of temperature-dependent spectral behaviors could provide a powerful tool for remote sensing of ice temperatures, if used in conjunction with a multiple scattering radiative transfer model. The Hapke model (e.g., Hapke 1981, 1993) is ideal for this purpose, as it has achieved widespread acceptance and an inexpensive computer can evaluate the model quickly over a wide range of parameter space. Finally, infrared array detector technology has advanced to the stage where high-quality near-infrared spectra of icy satellites can now be obtained relatively quickly at telescopes of modest aperture. With all these elements finally in place, we felt it was time to revisit the issue of near-infrared remote sensing of ice temperatures. In support of this effort, we undertook a campaign to obtain spectra of a number of icy outer Solar System objects.

OBSERVATIONS

The spectra presented in this paper were obtained at Lowell Observatory's 1.8-m Perkins telescope on Anderson Mesa, during observing runs in 1995 and 1998. All observations made use of the low-resolution spectroscopic mode of OSIRIS (Ohio State Infra-Red Imaging Spectrometer, described by DePoy *et al.* 1993), which featured a grism (grating–prism combination) to split the wavelength range from 1.2 to 2.4 μm into three orders, coinciding approximately with the J, H, and K atmospheric windows, with a spectral resolution of about 700. The three orders were recorded simultaneously, providing a threefold gain in data-acquisition efficiency that permitted us to observe fainter objects at a smaller telescope than would otherwise have been feasible. The detector was a 256 × 256 NICMOS3 HgCdTe array. This array, as well as all optical elements and moving parts were enclosed within a dewar cooled with liquid N_2.

Each object observation consisted of a set of at least five consecutive exposures, with individual exposure times ranging from 30 to 300 s, depending on target faintness, down to about visual magnitude 15. For very bright objects, shorter subexposures were used to avoid saturation. These were coadded to make synthetic 30-s exposures. Prior to each exposure, the object was moved to a new position in the spectrograph slit. This dithering was essential for minimizing the deleterious effect of individual bad pixels as well as permitting exposures to be subtracted pairwise for initial removal of night sky lines.

Extraction of spectra from the 2D images was a difficult signal processing task, consisting of subtracting the sky signal and then integrating over the object signal. Sky subtraction proceeded as follows. First, most of the sky signal was removed by the pairwise subtraction of two object spectral images. This subtraction left a positive image and a negative image of the object superimposed on the residual sky signal cause by variation in the sky flux between the two images. The second step was to subtract the residual sky. This subtraction was done by robust fitting of a line to each column (wavelength) while taking care to exclude rows holding the object images. This line was then subtracted at each column, thus removing the last traces of the sky signal.

We integrated the object signal using an optimal extraction technique patterned after the treatment described by Horne (1986). The key to getting the most out of optimal extraction is in determining an accurate spatial profile and being able to accurately position the profile with respect to the object image. This process required several steps which yielded successively better spectral extractions. On the first pass the location of the spectrum was determined with a linear fit to the center of the profile as a function of column number. The full-width at half maximum (FWHM) of each column was computed and the mean was recorded for each order. Then, a fixed-width Gaussian was fit to each order using the width for that order but leaving the position and amplitude of the Gaussian as free parameters. These positions were then fit with a second-order polynomial which became the "true" centerline. On the second pass, a numerical profile was built up from the sample provided by each column. The drift of the profile with respect to the detector rows provided a high degree of subsampling of the actual profile. This master profile was then smoothed with the LOWESS algorithm (locally weighted scatterplot smoother, described by Cleveland 1985) to yield a final numerical profile that was used in the optimal extraction. This procedure worked very well to follow the actual profile without the need for a precise analytic form, but it did not follow minor wavelength-dependent changes in the point-spread-function within each order.

Wavelength calibration for each spectral order was achieved by means of a quadratic fit to the observed positions of telluric night sky emission lines, resulting in wavelength accuracy better than ± 0.0015 μm (± 15 Å).

To obtain ratio spectra, solar analog stars were observed, bracketing target object observations in both time and airmass. This bracketing was generally accomplished by using selected early G-type SAO stars within a degree or two of the target objects. Differences in effective temperature between these stars and the Sun or the combined effects of poor guiding and differential refraction at high airmasses could have resulted in spectral slopes across our wavelength range. We used additional observations of standard solar analogs, such as 16 Cyg B, BS 6060, HD 219018, SA 93-101, SA 107-684, SA 112-1333, SA 113-276, and SA 115-271, to rule out the possible presence of

TABLE I
Jovian System Targets

Object name	Julian date[a]	r (AU)	Subsolar latitude	Solar analog stars observed
Europa	50996.987	4.98	1.73°	BS 6060, SA 115-271, Io
	50998.968	4.98	1.74°	BS 6060, SA 115-271, Io
Ganymede	50998.959	4.98	1.74°	BS 6060, SA 115-271, Io
	51002.903	4.98	1.76°	SA 115-271, HD 219018
	51003.900	4.98	1.76°	16 Cyg B, SA 112-1333, SA 115-271, Io
Callisto	50995.982	4.98	1.73°	BS 6060, SA 115-271
	51002.908	4.98	1.76°	SA 115-271, HD 219018

[a] Mean Julian date of object observations minus 2400000.

spurious spectral slopes. These additional solar analog stars, observed over a wide range of airmasses, were also useful in constraining telluric extinction. Tables I, II, and III list the times of our observations, along with the solar analog stars observed.

The spectrograph slit, 3×54 arcsec, was oriented North–South on the sky. Full width at half maximum seeing at the Perkins telescope ranged from about 1 to 3 arcsec, and was usually near 1.5 arcsec. Pointing errors of up to an arcsec combined with the seeing conditions to result in a nonnegligible and time-variable fraction of incoming object light being blocked by the slit jaws, rendering absolute photometric calibration impossible. When an object was not well centered in the spectrograph slit, a slope was produced across each spectral order relative to the spectrum of a well-centered or extended source. These order slopes resulted from an optical effect within the spectrometer, and should not be confused with the slopes across the entire spectral range resulting from external effects discussed earlier. Within each group of spectra of a target, order slopes of individual spectra were corrected to the group mean. Group slope corrections were then determined by comparing spectra of different objects around 1.45 μm, where data from both J and H orders overlapped. These corrections were applied to all three orders, resulting in excellent agreement between different sets of spectra of the same object, across all three orders.

For a block of observations obtained over a period of a few hours, the solar analog star spectra were used to calculate differential extinction as a function of wavelength. This extinction spectrum was used to correct each stellar spectrum to the airmass of each object exposure. Each object spectrum was normalized and then divided by the normalized average of all the stellar spectra corrected to the same airmass. This procedure eliminated telluric and solar absorptions, producing normalized albedo spectra of the target objects.

TABLE II
Saturnian System Targets

Object name	Julian date[a]	r (AU)	Subsolar latitude	Solar analog stars observed
Rings	50827.713	9.36	−14.2°	Hyades 64, SA 115-271, SA 93-101
	51003.980	9.32	−17.2°	16 Cyg B, SA 115-271, SAO 92781, Io
Enceladus	50827.602	9.36	−14.2°	Hyades 64, SA 115-271, SA 93-101
	51011.956	9.31	−17.3°	BS 6060, SA 112-1333, SAO 92781
Tethys	50827.632	9.36	−14.2°	Hyades 64, SA 115-271, SA 93-101
Dione	50827.663	9.36	−14.2°	Hyades 64, SA 115-271, SA 93-101
	51009.991	9.31	−17.3°	BS 6060, SAO 92781
	51010.997	9.31	−17.3°	BS 6060, SAO 92781
	51012.935	9.31	−17.3°	BS 6060, SAO 92781
Rhea	50827.645	9.36	−14.2°	Hyades 64, SA 115-271, SA 93-101
	51008.944	9.31	−17.3°	HD 1835, SAO 92781
	51010.970	9.31	−17.3°	BS 6060, SAO 92781
	51012.964	9.31	−17.3°	BS 6060, SAO 92781
	51013.938	9.31	−17.3°	SAO 92781
Iapetus	50997.981	9.32	−17.1°	SAO 92781
	51009.965	9.31	−17.3°	BS 6060, SAO 92781

[a] Mean Julian date of object observations minus 2400000.

TABLE III
Uranian System Targets

Object name	Julian date[a]	r (AU)	Subsolar latitude	Solar analog stars observed
Umbriel	49921.764	19.7	−49.7°	SAO 141651
	50994.917	19.9	−38.0°	SAO 163972
	50995.908	19.9	−38.0°	BS 6060, SA 115-271, SAO 163972
	51009.856	19.9	−37.9°	BS 6060, SAO 163972
Ariel	49920.859	19.7	−49.7°	16 Cyg B, SAO 141651
	49921.839	19.7	−49.7°	SAO 141651
	51010.866	19.9	−37.8°	BS 6060, SAO 163972
Titania	49919.769	19.7	−49.7°	SAO 141651
	49920.866	19.7	−49.7°	SAO 141651
	49922.761	19.7	−49.7°	SAO 141651
	50997.905	19.9	−38.0°	BS 6060, SAO 163972
	50998.891	19.9	−38.0°	BS 6060, SA 115-271, SAO 163972
	51011.844	19.9	−37.8°	BS 6060, SA 112-1333, SAO 163972
Oberon	49920.748	19.7	−49.7°	SAO 141651
	50991.933	19.9	−38.0°	BS 6060, SAO 163929
	50992.888	19.9	−38.0°	BS 6060, SAO 163972
	50993.906	19.9	−38.0°	SA 112-1333, SAO 163972
	50996.903	19.9	−38.0°	BS 6060, SA 115-271, Io, SAO 163972
	51013.859	19.9	−37.8°	BS 6060, SA 112-1333, SAO 163972
	51019.887	19.9	−37.7°	SAO 163972

[a] Mean Julian date of object observations minus 2400000.

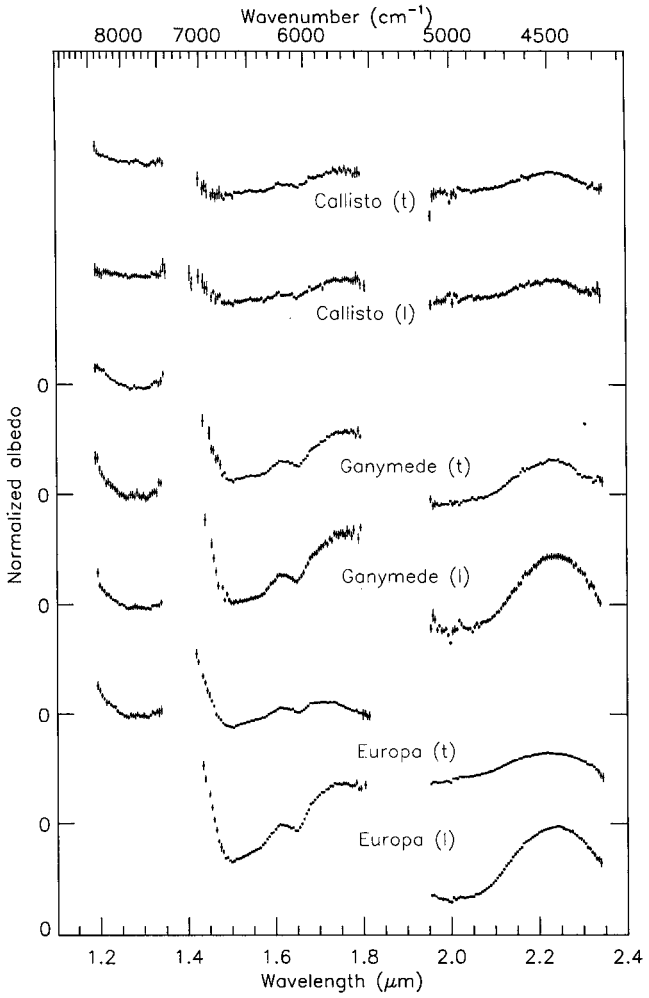

FIG. 1. Spectra of leading and trailing hemispheres of jovian satellites Europa, Ganymede, and Callisto, offset vertically with zero points indicated by tick marks. The spectra were normalized to the average between 1.2 and 1.3 μm. Formal error bars are shown, but are difficult to see because many are smaller than the plotting symbols.

The signal-to-noise ratio (SNR) of each object albedo spectrum was calculated from the scatter relative to the grand average for that object. The object albedo spectra were then combined by binning all the spectra for each object into 0.005 μm (50 Å) bins, each spectrum weighted by its SNR. Formal errors for each wavelength bin were calculated from the variance of data contributing to that bin.

Normalized albedo spectra of jovian, saturnian, and uranian satellites are plotted in Figs. 1, 2, and 3. The formal errors (indicated by vertical error bars, often difficult to discern because of their small sizes) appear to slightly overestimate the actual signal precision. The main sources of systematic error missing from the formal errors appear to be short term fluctuations in telluric extinction (particularly due to absorption by water vapor and CO_2) and variations in sensitivity across the NICMOS3 chip, which are not perfectly corrected by pairwise subtraction and flat fielding.

All of the spectra exhibit prominent H_2O ice absorptions. The saturnian and uranian system spectra share the characteristic absorption features of low temperature crystalline ice: a box-bottomed band at 1.53 μm and a narrower band at 1.65 μm. Neither amorphous H_2O ice nor hexagonal ice near its melting point have these features (Schmitt *et al.* 1998, Grundy and Schmitt 1998). Compared with the saturnian and uranian spectra, the jovian system spectra have relatively weak absorptions at 1.65 μm, and more rounded 1.53 μm bands, consistent with warmer H_2O ice. H_2O absorption bands are generally stronger for the leading hemispheres of the satellites observed. The spectrum of Enceladus is peculiar, in that its 1.65 μm band is deeper

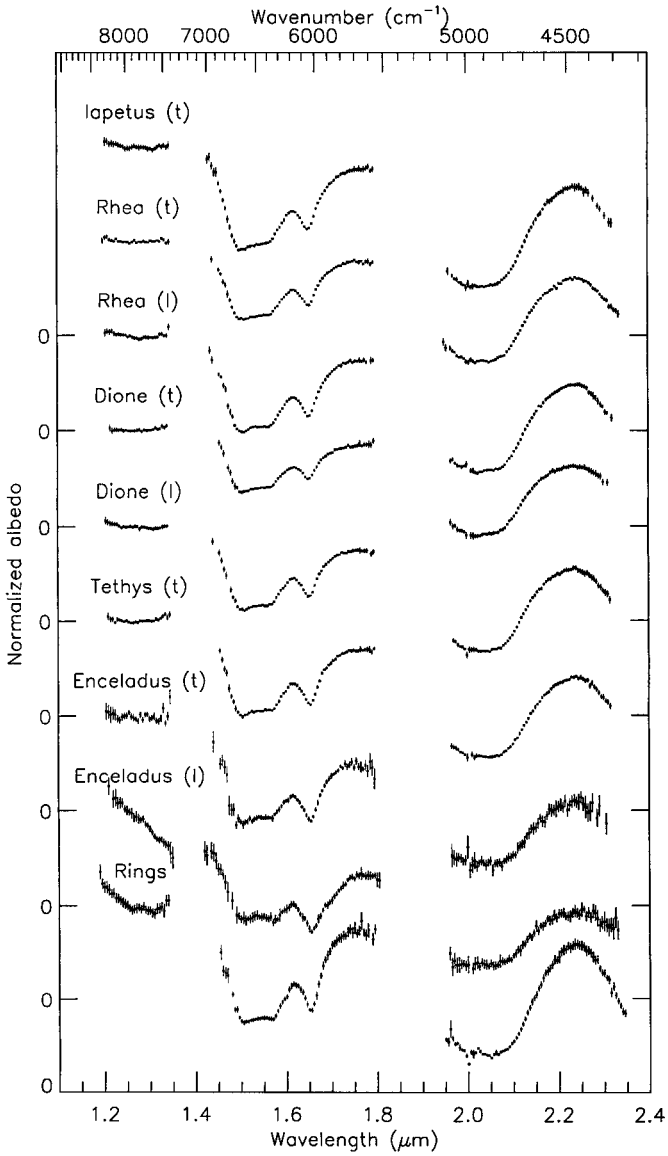

FIG. 2. Normalized spectra of saturnian rings and satellites. Note the differences in depth of H_2O absorptions between leading and trailing hemispheres, with bands being consistently deeper in leading hemisphere spectra. Formal error bars are shown, but many are smaller than the plotted points.

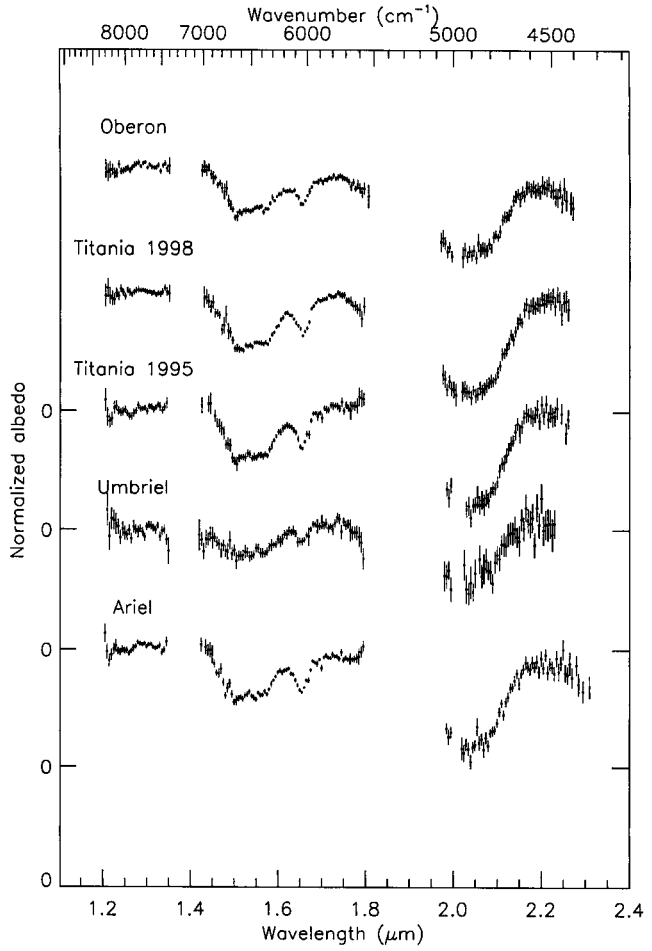

FIG. 3. Normalized spectra of uranian satellites. Formal error bars are shown. Umbriel, at visual magnitude 15, was the faintest object for which we were able to obtain sufficient SNR to clearly see the H_2O absorptions.

than its 1.53 μm band, for both hemispheres. This feature is not seen in ordinary hexagonal H_2O ice at any temperature.

ANALYSIS

To interpret our spectra, we made use of new temperature-dependent absorption coefficient data from Grundy and Schmitt (1998). We sought to take advantage of the suite of temperature-dependent spectral behaviors reported by these authors in an effort to derive H_2O ice surface temperatures from our reflectance spectra of various icy targets.

We needed a radiative transfer model to calculate synthetic albedo spectra from the new laboratory data. The Hapke model (Hapke 1981, 1993) was ideal for this purpose. This model accounts for the effects of multiple scattering of light in a particulate surface, especially important in surfaces composed of granular, transparent materials such as ice, where single scattering albedos are high and photons are able to undergo large numbers of scattering events prior to being absorbed or escaping from the surface. Details of our implementation of this model are published elsewhere (Grundy 1995). The surface of a solid body is divided into a series of flat tiles. At each wavelength, the bidirectional reflectance is calculated for each illuminated tile visible to the observer, and then the contributions of these tiles are projected-area-weighted and summed to simulate the flux arriving at the observer's location. Finally, the resulting high-spectral-resolution model spectrum is resampled at the wavelengths and spectral resolution of the observed data. The χ^2 goodness-of-fit can then be evaluated and an iterative procedure used to adjust the temperature and other model parameters to minimize χ^2.

Figure 4 shows three Hapke model spectra, illustrating the spectral effect of different ice temperatures. The 1.65-μm band is the spectral feature most obviously sensitive to temperature, but other wavelengths are temperature sensitive as well. For example, the wavelength of the absorption edge around 1.5 μm shifts with temperature, as does the wavelength of the 2-μm band and the shape of the 1.8-μm continuum region. The narrow band at 1.31 μm becomes deeper with decreasing temperature, much as the 1.65-μm band does. These various temperature dependencies provide a way to test the consistency of derived temperatures—each spectrum can be sampled into several subspectra and the best-fit temperature determined separately for each subspectrum.

In addition to the temperature, physical parameters such as the grain size of the ice and the abundance and nature of continuum absorbers are unknown *a priori*. Assumptions can be made about these parameters or they may be left as free parameters to be adjusted in concert with the ice temperature to minimize χ^2. The choice of parameters can influence the final result. We tried four

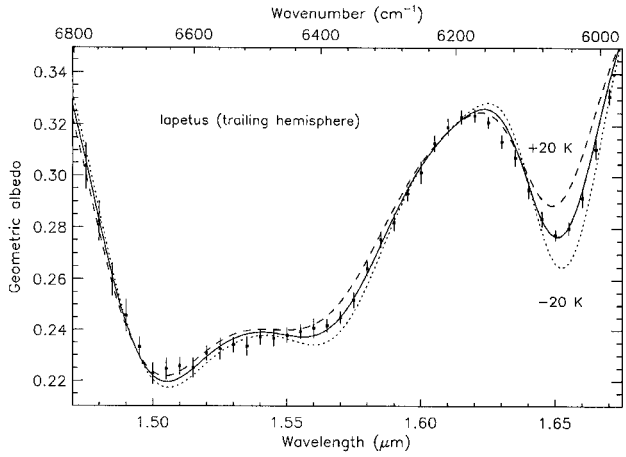

FIG. 4. Model 1 spectra (smooth curves) compared with our spectrum of the trailing hemisphere of Iapetus (points with error bars). The solid curve was calculated for H_2O ice at 97 K. Also shown are model spectra for ice temperatures 20 K warmer and colder, to illustrate the temperature sensitivity of the absorption bands. All three models fail to fit the observed spectrum near 1.63 μm, possibly due to the presence of of some contaminant with an absorption band in that region.

different scenarios to explore the sensitivity of the derived temperature to our model assumptions. Model 1 is a globally homogeneous intimate mixture of ice and a spectrally neutral continuum absorber with the same grain size as the ice and a Lambert absorption coefficient of 100 cm^{-1}. The three free parameters are the grain size, the mixing ratio, and the ice temperature. Model 2 is similar, but with the assumption of the spectral neutrality of the continuum absorber relaxed. One additional free parameter adjusts the continuum absorber's spectral slope. Model 3 is similar to the first, with the addition of spectrally neutral, ice-free patches on the surface. Two additional free parameters are the fractional area and the albedo of these regions. Model 4 is also similar to the first, except that instead of equant, smooth-surfaced grains, the grains are assumed to have extremely rough exteriors, as if a fine-grained frost had condensed on them. The relative amount of ice in the interiors of grains versus in their rough exteriors is the additional free parameter in this model.

These four models are not particularly complex nor realistic, as their objective is simply to determine ice temperatures and to investigate the sensitivity of those temperatures to model assumptions. They do not account for the broad diversity of terrains on any real Solar System body, isotropic multiple scattering is assumed, and they use the Hapke model's *ad hoc* backscattering function (Hapke 1993). These simplifications are justified because we are not seeking to determine textural or compositional details. For that purpose, more sophisticated models would be needed, as have recently been fitted to spectra of a few icy satellites (e.g., Benedix *et al.* 1998, Roush *et al.* 1998a, 1998b). Analysis of compositional and textural implications of our spectra is left to future work.

All four models require additional photometric parameters, such as single scattering phase functions $P(g)$, mean surface roughness angles $\bar{\theta}$, and Hapke backscattering parameters B_0 and h. Geometric albedos A_p were also needed for scaling our reflectance data. We fixed these parameters to values for near-infrared or visible wavelengths from Esposito *et al.* (1984), Buratti (1985), Buratti *et al.* (1990), Helfenstein *et al.* (1991), Calvin *et al.* (1995), Domingue *et al.* (1995), Karkoschka (1997), Cruikshank *et al.* (1998), and Verbiscer and Helfenstein (1998). Where certain parameters were not available for a particular satellite, values were estimated or taken from similar satellites.

To check consistency, we took seven subsamples of each spectrum (e.g., just the J order, just the H order, or just the K order), and fit each of our four models to each of these subspectra, resulting in 28 fits for each original spectrum. To obtain temperatures from these fits, we evaluated contours of constant χ^2 in free-parameter space, using the method of Lampton *et al.* (1976). For each model fitted to each subspectrum, the 68% confidence contour interval enclosed a range of temperatures which could be expressed as a single temperature with an associated one-sigma error bar. Two examples are shown in Fig. 5. These temperatures were combined, and the results were tabulated in Table IV, along with errors reflecting the scatter of temperatures for different models and wavelength ranges. Models which resulted in poor spectral matches were excluded, as indicated by gray points in Fig. 5.

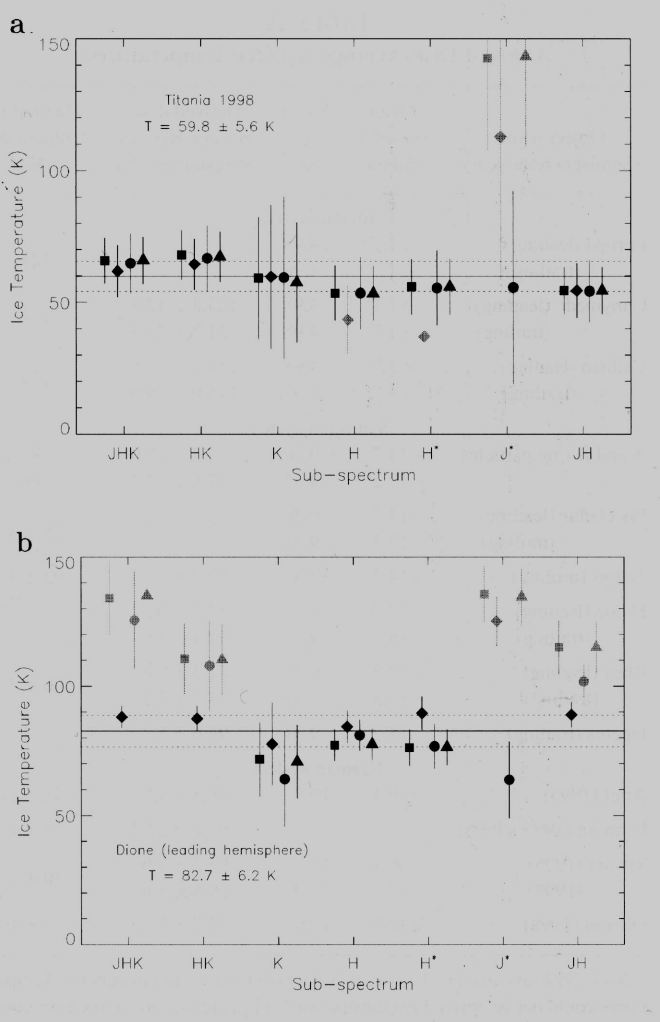

FIG. 5. Examples of temperatures derived from fitting the four models described in the text to seven different subspectra of (a) Titania and (b) Dione. Fits from Models 1–4 are represented with squares, diamonds, circles, and triangles, respectively. The seven subspectral ranges are indicated along the abscissa, labeled according to which spectral orders contributed data. H* indicates a narrow window from 1.55 to 1.72 μm, enclosing the 1.65 μm band. J* indicates subspectra with wavelength limits 1.15 to 1.55 μm. Gray points represent combinations of models and wavelength ranges which gave clearly spurious results (poor matches to the observed spectrum) and were rejected. Poor fits to the spectrum of Dione were more frequent than for Titania, suggesting that the surface texture and/or composition on Dione may be more complex than the models used in this paper are capable of simulating, or that nonhexagonal H_2O plays a more significant role on Dione's surface. The temperatures and error bars indicated by horizontal lines were calculated based on the distribution of temperatures derived from models which appeared to give reasonable fits to the observed spectra.

Poor fits can result from a number of situations. The presence of a spectrally sloped continuum absorber leads to poor fits with Models 1, 3, and 4, since they only include spectrally neutral continuum absorption. As shown in Fig. 6, application of the models to the full spectral range (the first subspectrum,

TABLE IV
Derived Disk-Average H_2O Ice Temperatures

Object name (hemisphere or year)	Mean subsolar latitude	Mean r (AU)	Derived disk-average H_2O ice temperature (K)	Thermal IR temperature (K)
		Jovian system		
Europa (leading)	+1.7°	4.98	—	121
(trailing)	+1.7°	4.98	—	
Ganymede (leading)	+1.7°	4.98	125.8 ± 12.3	139
(trailing)	+1.7°	4.98	121.7 ± 23.6	
Callisto (leading)	+1.7°	4.98	114.3 ± 16.6	154
(trailing)	+1.7°	4.98	115.0 ± 20.0	
		Saturnian system		
A and B ring particles	−14.2°	9.36	70.4 ± 10.0	82
	−17.2°	9.32	77.6 ± 12.4	86
Enceladus (leading)	−14.2°	9.36	—	75 ± 3
(trailing)	−17.3°	9.31	—	
Tethys (trailing)	−14.2°	9.36	68.7 ± 7.5	93 ± 4
Dione (leading)	−17.3°	9.31	82.7 ± 6.2	—
(trailing)	−15.8°	9.34	90.4 ± 7.0	
Rhea (leading)	−17.3°	9.31	81.6 ± 3.6	100 ± 2
(trailing)	−16.3°	9.33	88.2 ± 7.2	
Iapetus (trailing)	−17.2°	9.31	96.6 ± 5.4	—
		Uranian system		
Ariel (1995)	−50.1°	19.7	58.8 ± 12.2	71 ± 14
Umbriel (1995+1998)	—	—	63.6 ± 27.2	69 ± 10
Titania (1995)	−50.1°	19.7	63.1 ± 5.6	70 ± 7
(1998)	−37.7°	19.9	59.8 ± 5.6	
Oberon (1998)	−37.7°	19.9	72.7 ± 12.2	70 ± 10

Note. Disk-average H_2O ice temperatures derived from our spectra. Temperatures could not be derived for Europa nor for Enceladus, due to the peculiarity of their spectra. For comparison, thermal infrared temperatures are shown in the last column. For jovian satellites, these temperatures are 20-μm full-disk brightness temperatures from Morrison *et al.* (1972). For saturnian rings, they are 20-μm brightness temperatures from Esposito *et al.* (1984) Fig. 31a, and for saturnian satellites they are subsolar point temperatures from Hanel *et al.* (1982) and Cruikshank *et al.* (1984), based on Voyager IRIS observations at 50 μm. For the uranian satellites, they are full-disk brightness temperatures calculated from Q filter fluxes reported by Brown *et al.* (1982).

labeled "JHK" in Fig. 5) can produce poor fits, as many of our spectra have K albedos lower than would be expected for pure H_2O, possibly due to the presence of another absorber or to a grain size distribution effect not amenable to simulation by our simple models (e.g., Grundy and Fink 1994, Grundy 1995). Fits to Ganymede spectra were generally poor, except for Model 3, consistent with a significant spectral contribution from ice-free terrain. Poor fits can also result from H_2O in phases other than hexagonal ice, as will be discussed later. Poor fits were especially notable for Europa and Enceladus, which have peculiar spectral characteristics quite unlike those of ordinary ice-I_h.

We emphasize that ice temperatures derived from spectra of unresolved satellites are disk-average ice temperatures, with light reflected from regions over the entire visible hemisphere contributing to the observed spectrum in proportion to their albedos and projected areas. Naturally, the surface temperature varies considerably over a hemisphere, due to differences in latitude, longitude, local slope, and albedo, not to mention possible regional variations in thermal properties due to texture, composition, etc. Furthermore, thermal emission from low-temperature H_2O ice is mainly emitted in the 20–100 μm range. The optical properties of H_2O ice cause this emission to originate from the uppermost few micrometers, i.e., from the very first layer of grains, considerably more shallow than the millimeter to centimeter mean depths at which solar radiation is absorbed. The result is a solid-state greenhouse, a vertical thermal gradient with greater temperatures at depth (e.g., Brown and Matson 1987, Matson and Brown 1989, Urquhart and Jakosky 1996). Since light penetrates more deeply into a surface at wavelengths where the single scattering albedo is high, high-albedo portions of the spectrum generally sample to greater depths. So temperatures derived from the 1.31-μm band could be appropriate for a greater depth than the temperatures derived from the 1.53-, 1.65-, and 2-μm bands. Unfortunately, with full-disk spectra at modest SNR we cannot hope to separate temperature variations between different regions and different strata in the surface. This level of analysis may, however, become possible with spatially resolved, high precision spectra from spacecraft instruments.

INTERPRETATION

To interpret our disk-average H_2O ice temperatures, we employed thermal models to compute theoretical temperature distributions from which we could compute disk-average temperatures by integrating over the visible disk, weighting by the projected area. Two "standard" thermal models, the "fast-rotator" and the "slow-rotator" have been widely used (e.g., Lebofsky and Spencer 1989). These models require few free parameters and are easily calculated. The slow-rotator model assumes negligible thermal inertia, so that the temperature of each point on the surface can be derived from the instantaneous balance of absorbed and emitted radiation. The opposite extreme of high thermal inertia is assumed in the case of the fast-rotator model, in which temperatures are derived from the diurnally averaged balance between absorption and radiation. If the Sun is located along the spin axis of a spherical body, these two models give identical results, but differences emerge when the spin axis is pointed elsewhere. For such geometry, the mean surface temperature (as seen from the direction of the Sun) is lower for the fast rotator model, because heat is radiated from both day and night sides in that model. The greatest difference is seen when the Sun lies in the object's equator plane, but even for the case of the uranian system, where subsolar latitudes during our observations were as high as 50° and 38°, in 1995 and 1998, respectively, the differences between fast- and slow-rotator model temperatures are significant. In general, the fast-rotator model is more applicable at greater heliocentric distances where lower

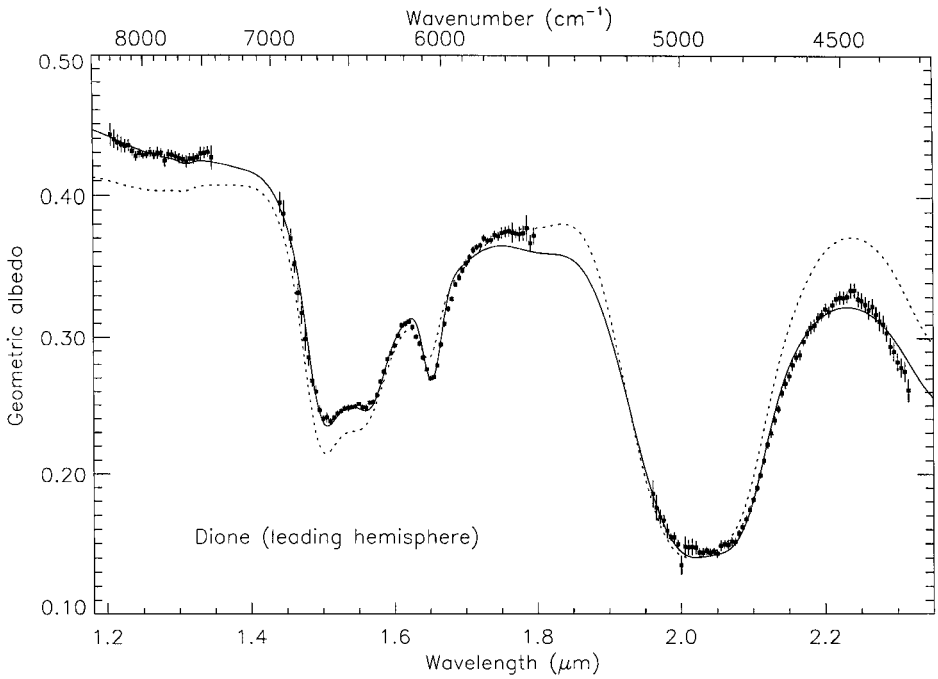

FIG. 6. Example of two fits to the leading hemisphere spectrum of Dione. The dotted curve is the fit for Model 1, obviously a poor fit, as it fails to match the band depths at 1.53 and 1.65 μm and the continuum slope from J through K. The solid curve is the fit for Model 2, which provides a much closer match to the continuum slope and the H_2O band depths.

temperatures make radiative cooling less efficient (Sykes *et al.* 1987, Spencer *et al.* 1989).

Our satellite ice temperatures are shown in Fig. 7, versus equilibrium temperature for unit emissivity,

$$T_{\text{equilibrium}} = \sqrt[4]{\frac{(1 - A_b)S_\odot}{\sigma r^2}},$$

where A_b is the bolometric bond albedo, $S_\odot$ is the solar constant, σ is the Stefan–Boltzmann constant, and r is the heliocentric distance. All of our satellite H_2O ice temperatures fall a bit below the slow-rotator model line. This is not surprising; an ice temperature above the slow-rotator line would be very difficult to explain without an implausibly low emissivity. For granular water ice, the thermal infrared emissivity should be near unity (e.g., Spencer 1987a).

Two effects cause ice temperatures to be lower than predicted by the slow-rotator model. First, as noted earlier, thermal inertia allows radiative cooling of the night side to reduce temperatures on the visible day side. The maximum possible temperature reduction from this mechanism is the difference between fast- and slow-rotator lines on Fig. 7. The temperature reduction is less for nonequatorial illumination. Second, segregation of ice from darker materials results in brighter, ice-rich regions absorbing less solar energy and remaining colder than neighboring darker patches. The temperature reduction from this mechanism can be substantial, since clean, fine-grained ice can have a high bolometric bond albedo and thus absorb very little solar energy. Unlike thermal emission measurements, our ice temperature sensing technique is most sensitive to the cleanest, brightest icy patches.

Active segregation of ice from darker, less volatile materials was anticipated for Ganymede and Callisto, based on thermal segregation models (Spencer 1987a, 1987b). These models show that for ice temperatures above ~110 K, differential sublimation rapidly transfers ice from darker, warmer, ice-poor regions to colder, brighter, ice-rich regions. High-contrast albedo patterns consistent with ice segregation, by thermal or other processes, have now been observed in high-resolution Galileo images of Ganymede (Prockter *et al.* 1998) and Callisto (Moore *et al.* 1999).

Spencer (1987a, 1987b) noted that this style of thermal segregation was unlikely on saturnian and uranian satellites, because of their lower temperatures and much lower ice sublimation rates. At lower temperatures, thermal radiation is less efficient, so for a given thermal inertia and rotation rate, more of the total emission is radiated from the night side. Day side surface temperatures are thus lower than predicted by slow-rotator models. Our ice temperatures for Ariel and Titania (58.8 ± 12.2 Ariel in 1995, 63.1 ± 5.6 Titania in 1995, and 59.8 ± 5.6 K Titania in 1998) are about 1σ below even fast-rotator disk-average temperatures (67.8, 68.6, and 65.4 K, respectively). These low ice temperatures suggest that ice is somewhat segregated even on the surfaces of these bodies. Polar temperatures on uranian satellites are strongly seasonal, due to high obliquity, but they never approach the range where thermal segregation becomes efficient.

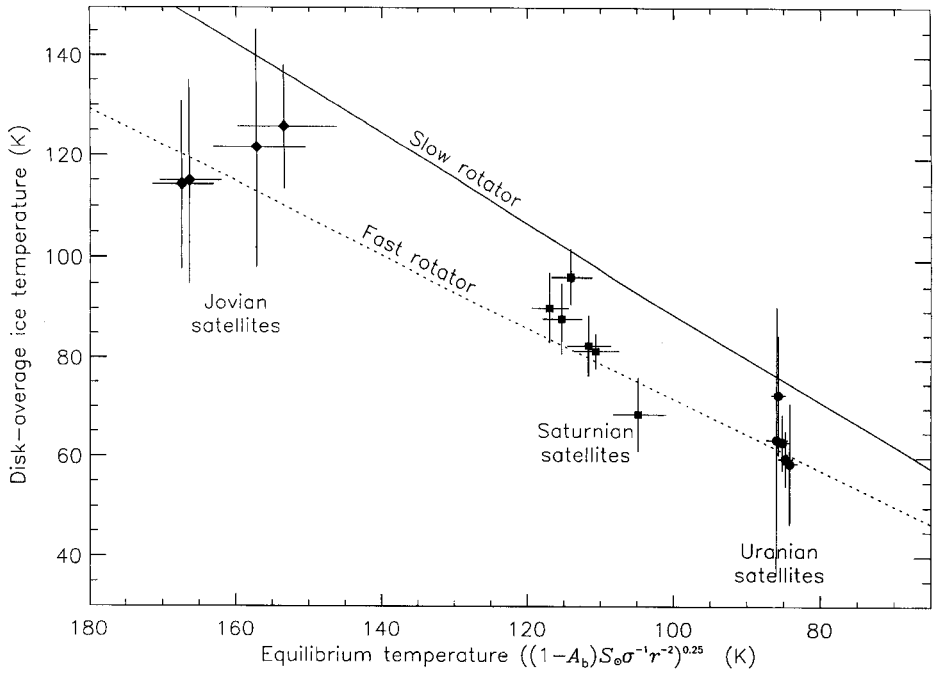

FIG. 7. Disk-average ice temperatures from our satellite spectra, plotted versus equilibrium temperature for global bolometric bond albedos calculated from the literature. The solid line is the locus of points consistent with disk-average temperatures calculated for the temperature distribution of the slow-rotator thermal model. The dotted line is for the fast-rotator model, viewed equator-on. As viewed from other latitudes, this line shifts toward the slow-rotator curve, until they coincide for pole-on orientation. All of our satellite ice temperatures fall below the slow-rotator line.

So for ice to be segregated on the surfaces of Ariel and Titania, either the pattern must be a relic of an earlier time, when their surfaces were geologically active, or a process other than thermal mobilization must be at work.

One can also compare our results with temperatures determined from infrared thermal emission measurements, as tabulated in the last column of Table IV. Unfortunately, these thermal emission temperatures are completely different entities from our disk-average ice temperatures, having been obtained at different epochs, with different illumination and observation geometries, and being sensitive to different aspects of the surface temperature distribution. Wavelength-integrated thermal emission goes as T^4, so full-disk brightness temperatures tend to be dominated by the warmest temperatures, generally on low-albedo, Sun-facing slopes and in the vicinity of the subsolar point or the pole, depending on thermal inertia, period, and subsolar latitude. Our disk-average ice temperatures sample the surface such that each illuminated, visible element of the surface contributes in proportion to its projected area and bidirectional reflectance, so the highest albedo, coldest regions contribute the most. With this caution in mind, our disk-average ice temperatures are, as expected, systematically lower than full-disk brightness temperatures of jovian and uranian satellites derived from ground-based thermal IR observations (e.g., Morrison *et al.* 1972, Brown *et al.* 1982) and from local maximum temperatures of saturnian satellites derived from Voyager spacecraft data (e.g., Hanel *et al.* 1982, Cruikshank *et al.* 1984). Local maximum temperatures are warmer than full-disk brightness temperatures, and can be converted by means of a thermal model. For example, a local maximum temperature of 100 K converts to 20 μm full-disk brightness temperatures of 84.7 and 93.4 K, for the slow- and fast-rotator thermal models, respectively, and to disk-average temperatures of 89.0 and 95.4 K, for the geometry of the saturnian system in 1998.

For the uranian system, much of the difference between brightness temperatures and ice temperatures can be attributed to differences in geometry if the thermal inertia is not zero. During the early 1980s, Uranus was closer to the Sun and oriented nearly pole-on, in contrast with the present, with the subsolar latitude rapidly approaching the equator. The fast-rotator model applied to Titania results in full-disk 20 μm brightness temperatures of 78.5, 74.2, and 72.0 K, and disk-average temperatures of 75.7, 68.6, and 65.4 K in 1982, 1995, and 1998, respectively.

The situation is more complex for Saturn's rings, where the thermal infrared brightness temperature varies with the angle of solar elevation above the ring plane. Our A and B ring ice temperatures fall about 10 K below the apparent trend for 20 μm B ring brightness temperature as a function of opening angle (Esposito *et al.* 1984). A lower temperature for H_2O ice is consistent with some diversity in the albedos of ring particles, with darker, warmer particles (perhaps derived from exogenous sources) contributing a disproportionate share of the thermal emission. However, the Hapke model assumes particles in relatively close proximity to one another, so while it may give

reasonable results for individual ring particles, it is not strictly applicable to an optically thick medium such as the ring environment, where particles are widely separated. Our ring particle ice temperatures should thus be interpreted with somewhat less confidence than our satellite ice temperatures.

Finally, we tested the possibility of discriminating between spatial temperature distributions predicted by different thermal models from spatially unresolved spectra of ice-covered satellites. We generated synthetic spectra for spheres obeying the two standard thermal models and for an isothermal sphere. All three temperature distributions were set up so that they had the same disk-average mean temperature of 100 K. Each model consisted of a sphere represented by 320 tiles, each covered with dirty ice at the appropriate temperature. The spectral contributions of all visible tiles were calculated and then combined to produce synthetic spectra. These spectra differed negligibly, with differences comparable to the line thickness in Fig. 4. So with disk-integrated spectra, even at very high spectral resolution and SNR, it is not possible to distinguish between the two thermal models, or even to distinguish a realistic temperature distribution from an isothermal surface. Spatially resolved spectral or thermal mapping offers the only possibility of mapping the ice temperature distribution over the surfaces of these satellites.

POTENTIAL PROBLEMS

Our method of determining temperatures from near-infrared spectra of icy surfaces is a potentially powerful technique, when good-quality IR spectra can be obtained. There are, however, potential pitfalls which should be pointed out. A number of other effects which shift the apparent wavelengths or shapes of the H_2O bands will result in errors in the derived temperature, if they are not properly accounted for. These effects are described in this section, and their likelihood of influencing our temperature results is assessed.

A continuum absorber which imparts a spectral slope will shift the apparent temperature, if the model being fitted to the data only includes spectrally neutral continuum absorption. It was for this reason that we included Model 2 among our 4 models. Figure 6 shows how Model 1 fails to match the full spectrum of Dione's leading hemisphere, while Model 2 provides a reasonable fit (the only usable fit for the full spectrum "JHK" in Fig. 5b).

Amorphous water ice, stable over geological time scales at temperatures up to ~110 K (Jenniskens *et al.* 1998), is spectrally similar to crystalline water ice near its melting point (e.g., Schmitt *et al.* 1998). Both warm hexagonal ice-I_h and cold amorphous ice have absorptions at slightly shorter wavelengths than those of low temperature ice-I_h and have no 1.65 μm band. With these spectral characteristics, a small quantity of amorphous ice mixed with or covering crystalline ice could result in erroneously high derived temperatures. Although no detection of amorphous ice has ever been reported for a satellite surface, it may condense from the vapor phase following impact vaporization, sputtering by energetic particles, or a cryovolcanic eruption.

Below 70 to 80 K, ultraviolet, electron, proton, and ion irradiation have been found to progressively transform crystalline ice into amorphous ice (Kouchi and Kuroda 1990, Heide 1984, Moore and Hudson 1992, Strazzulla *et al.* 1991). The rate of amorphization with the energy dose strongly decreases with increasing temperature, however, reaching negligible values above about ~80 K, a temperature where the atomic, molecular, and ionic species produced by irradiation (and suspected to cause the amorphization) tend to react and/or escape efficiently from the crystal lattice. The depth of radiation amorphization of a surface depends on the penetration depth of the radiation, from less than a micrometer for UV photons and solar wind protons (KeV) to several tens of micrometers for magnetospheric ions and Galactic protons (MeV) and even deeper for larger atomic nuclei. If the temperature of a surface never exceeds about 70 K, this layer may accumulate, but if the surface temperature ever reaches 80 K or above, there is probably no radiation-induced amorphous ice at the surface. This effect is thus probably restricted to the coldest and most strongly irradiated regions of the coldest outer Solar System objects, perhaps including brighter equatorial regions on the uranian satellites, as well as Neptunian satellites and trans-Neptunian objects.

Traces of high-pressure phases of H_2O ice produced by impact shock and subsequent quenching (e.g., Gafney and Matson 1980) could also result in subtle band shifts and temperature errors. For example, ices VI and VII have 2-μm bands at significantly shorter wavelengths than low-pressure hexagonal ice-I_h (Kato *et al.* 1992). These high-pressure phases are unstable on exposure to vacuum, but at uranian and saturnian satellite surface temperatures, they may be able to survive over geologically significant time scales. The efficiencies of impact creation, quenching, and deposition of high-pressure phases in the optically active uppermost surface layers are unknown.

Cubic H_2O ice-I_c, meta-stable at temperatures up to about 140 K, may also be found on the surfaces of icy satellites, but two lines of evidence suggest that the temperature-dependent spectral behavior of cubic ice is indistinguishable from that of ice-I_h in our wavelength range, and thus should not interfere with our temperature determinations. The first is near-infrared laboratory work which has not yet been published (B. Schmitt, personal communication, 1998). The second is that no differences are observed between cubic and hexagonal ices in the mid-infrared (Bertie and Whalley 1964, Taylor and Whalley 1964, Hardin and Harvey 1973), and only minor differences are observed in the far-infrared, where the effects of crystal structure are particularly important (Bertie and Jacobs 1977). Since the near-infrared absorptions are overtones and combinations of mid-infrared fundamental vibrational modes, identical spectral behavior in the mid-infrared region implies identical spectral behavior in our spectral region.

Another possible source of errors in derived temperatures is the presence of modest quantities of bound water, as occurs in hydrated evaporite or phyllosilicate minerals. Bound water generally exhibits absorptions at wavelengths shorter than those

of hexagonal or amorphous ices and does not show a 1.65-μm band. Minor quantities of such materials mixed with hexagonal ice could be mistaken for pure hexagonal ice at a somewhat higher temperature, particularly at lower spectral resolutions. These types of materials are cosmochemically plausible (e.g., Kargel 1991) and a detection of these materials has recently been reported, based on Galileo NIMS spectroscopy of the surface of Europa (McCord *et al.* 1998, 1999). However, unique identifications are difficult, since, as discussed above, various effects produce similar spectral signatures (see also Dalton and Clark 1998).

Our spectra of Europa and Enceladus resulted in consistently poor fits to the observed spectra, preventing us from determining ice temperatures for those two bodies. Clearly, granular hexagonal H_2O ice is not the sole contributor to the shapes and positions of the H_2O absorption bands on Europa and Enceladus. The spectrum of Ganymede also resulted in poor fits for a number of model and subspectrum combinations. For Ganymede and Europa, the leading hemisphere spectra are less peculiar than those of the trailing hemispheres. This trend suggests that the unusual absorption bands may be related to the enhanced radiation bombardment of the trailing hemispheres of these bodies. Alternatively, higher rates of impact gardening on the leading hemispheres may be churning up cleaner ice. The opposite trend is seen with Enceladus, where the leading hemisphere spectrum is quite unusual, with a 1.65-μm band notably deeper than the 1.53-μm band, unlike hexagonal ice at any temperature. The trailing hemisphere shows the same effect, but to a lesser degree. If the phenomenon responsible for the peculiar spectrum of Enceladus also affects the spectra of other satellites, but to a lesser degree, it could result in derived temperatures below the actual H_2O ice temperatures.

TIME-RESOLVED EXPERIMENTS

While the mean temperature derived from near-infrared spectroscopy of ice may be influenced by the effects described above, a change in temperature of a particular surface should result in observable spectral changes relatively independent of these complicating factors. We undertook three experiments to search for possible temperature changes.

For the first experiment, we looked for seasonal temperature changes on Titania, using spectra obtained in 1995 and 1998. Over that time span, the subsolar latitude on Titania moved from $-50°$ to $-38°$, while the heliocentric distance increased from 19.7 to 19.9 AU. The small change in heliocentric distance should only result in a temperature drop of about 0.4 K, but for nonzero thermal inertia, a change toward more equator-on insolation should also result in a lower average surface temperature. For high thermal inertia (the fast-rotator model), the total expected mean temperature drop is 3.2 K. For most of the models and wavelength intervals, best-fit temperatures average about 3.3 K lower for the 1998 spectrum. The error bars, ± 5.6 K for both years, respectively, make it seem as if this is not a significant result, but it should be noted that these errors attempt to reflect the dominant systematic errors, which should affect both data sets in an identical manner. Formal errors based on contours in χ^2 space are more appropriate for evaluating the change in temperature, and these errors are only ± 1.9 and ± 2.4 K, for the 1995 and 1998 temperatures, respectively. The observed change in mean ice temperature thus appears to be a real effect, confirming that thermal inertia plays a significant role in moderating the surface temperature of Titania's H_2O ice. Alternatively, the observed temperature difference could be due to a sampling effect; while both spectra are averages over several nights, and thus sample a range of sub-Earth longitudes, the two spectra still sample different mixes of Titania's surface, particularly in the equatorial region.

In our second experiment, we looked for posteclipse warming of Ganymede using a sequence of spectroscopic observations following Ganymede's emergence from about 3.4 h in Jupiter's shadow on UT 1998 July 9. Ganymede was observed from UT 8:55:46 (about 7 min after the center of the disk emerged from Jupiter's shadow) until it approached the limb of Jupiter about 1.6 h later. Spectra of Ganymede were interspersed with spectra of Io, which served as the solar analog for this experiment. The use of Io's spectrum as a proxy for the solar spectrum in our wavelength region was validated by separate Io and solar analog star observations carried out on the same and other nights. As shown in Fig. 8, our data are suggestive of a several-degree warming trend during the 1.6 h of our observations, with most of the change occurring at the beginning of the posteclipse time period. Ignoring the first point, the average posteclipse ice temperature was about 6° colder than the temperature measured for Ganymede's leading hemisphere, but only 2° (well within experimental uncertainty) colder than the trailing hemisphere ice temperature. The nearly constant posteclipse ice temperature is strikingly different from the posteclipse evolution of the 20-μm full-disk brightness temperature reported by Morrison and Cruikshank (1973), suggesting very different thermal properties for the spectroscopically active uppermost millimeters of Ganymede's bright ice, compared with the darker materials that dominate the 20-μm thermal emission. Four thermophysical models are shown in Fig. 8, numbered in order of increasing thermal inertia. Our data are inconsistent with thermal models based on the nominal parameters of Brown and Matson (1987) and Matson and Brown (1989) or the scaled ice parameters of Urquhart and Jakosky (1996), curves 2 and 3, with thermal inertias of 1.2×10^4 and 3.7×10^4 erg cm^{-1} s$^{-0.5}$ K^{-1}, respectively. Our data require either a higher thermal inertia, $\sim 1.5 \times 10^5$ or higher, as in curve 4, or a very low thermal inertia, at most 800 erg cm^{-1} s$^{-0.5}$ K^{-1}, as in curve 1. The high thermal inertia solution is more plausible from a mechanical point of view, if sintering of H_2O ice grains results from solar heating over time. High thermal inertia ice is also consistent with the two-component model of Spencer (1987a), in which the brighter component had a high thermal inertia.

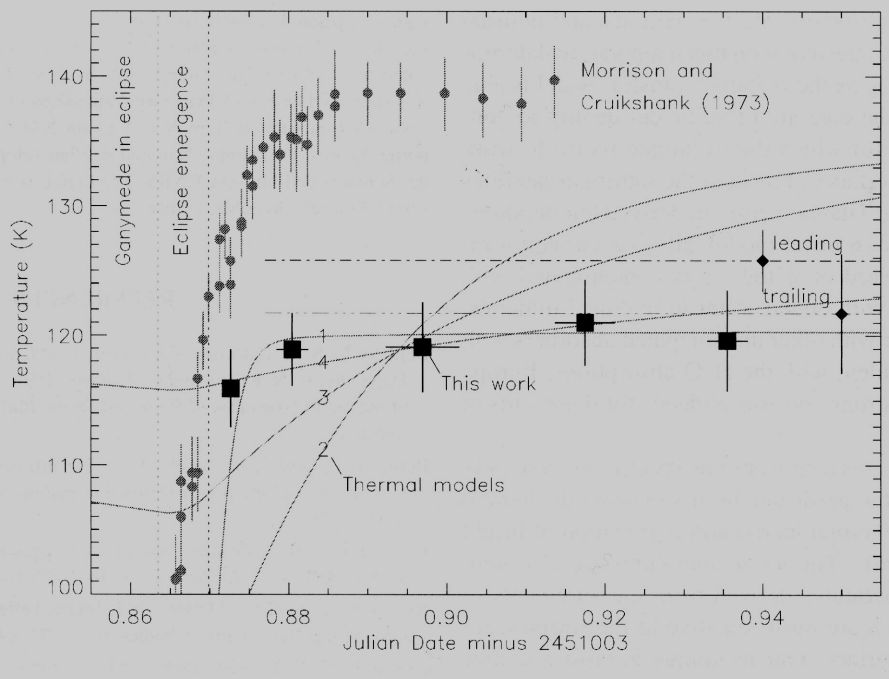

FIG. 8. Time-resolved disk-average ice temperature for Ganymede (squares) following emergence from 3.4 h in Jupiter's shadow. Horizontal error bars illustrate the time span over which data were obtained and vertical error bars show formal errors, which do not reflect possible systematic sources of error discussed in the text. The posteclipse ice temperatures are a few degrees colder than the ice temperature measured for Ganymede's leading hemisphere (dashed line at 125.8 K, measured at Julian date 2450998.959), but are consistent with the trailing hemisphere ice temperature (121.7 K, measured at Julian date 2451002.903), which was less well determined. While our data do suggest a very slight posteclipse warming trend, the disk-average ice temperature is considerably more stable than the posteclipse 20-μm full-disk brightness temperature history reported by Morrison and Cruikshank (1973), shown as gray points. Our data are inconsistent with thermal models based on thermal parameters assumed by Brown and Matson (1987) and Matson and Brown (1989), and by Urquhart and Jakosky (1996), shown as gray curves numbered 2 and 3, respectively. Gray curves 1 and 4 represent thermophysical models consistent with our data, with low- and high-thermal inertias, respectively, as described in the text.

We looked for post-eclipse warming of Saturn's ring particles in our third experiment, by placing the spectrograph slit as close as possible to Saturn's limb. We obtained spectra of the A and B rings after the particles passed behind Saturn, where they spent almost an hour shaded from the Sun. Unfortunately, our observing run was prior to opposition, so the ring particles were illuminated by sunlight for almost 20 min before they emerged from behind Saturn's limb and moved far enough away from the limb to be observed. The spectra obtained after emergence resulted in an ice temperature of 71.2 ± 2.5 K (again, this is the formal error which makes no attempt to account for systematic problems). For comparison, the spectrum derived from the other part of the spectrograph slit, where the ring particles had been exposed to sunlight for several hours, yielded an ice temperature of 77.6 ± 3.4 K, apparently a significant effect. This experiment should be repeated, however, as we only took eight exposures, of which we had to discard five, due to contamination by light from Saturn. A more sophisticated analysis is required as well, taking radiative transfer within the ring system into account.

The results of these three experiments are all consistent with significant thermal inertias. The average depth at which solar energy is absorbed in icy surfaces ranges from millimeters to a centimeter or more, while thermal emission escapes exclusively from the uppermost few micrometers. The result is a thermal gradient in the surface, with slightly higher temperatures at depth. Without an atmosphere, heat transport is predominantly by grain to grain conduction. The rate of conduction can be quite slow unless the contact area between adjacent grains is large, as in the case of sintered grains. At low outer Solar System temperatures, radiation contributes significantly to the heat transport only if the contact area between grains is extremely small, as in an unusually fluffy surface or in Saturn's rings. Our near-infrared temperature sensing technique is most sensitive to temperatures in the uppermost several grain diameters of the surface, at depths where heat is being transported upward, toward the cooler surface. More detailed models of heat transport in granular ice are required to better constrain the mechanical texture of H_2O ice on Titania, Ganymede, and Saturn's rings, based on our observational data.

CONCLUSION

We acquired new near-infrared spectra of a dozen icy satellites of Jupiter, Saturn, and Uranus, as well as the rings of Saturn. Making use of the temperature-dependent near-infrared spectral variation of H_2O ice in conjunction with a multiple scattering radiative transfer model, we were able to derive from our spectra ice temperatures with accuracies as high as $\pm$ several Kelvins.

The presence of other absorbers, ice-free regions, and unusual scattering effects do not interfere with this temperature determination technique, as long as the radiative transfer model is able to simulate them and the data are of sufficient quality to constrain them. Examples for which the technique seems to work quite well include the surfaces of most of the saturnian satellites and the uranian satellite Titania. Errors in derived temperatures can result if the radiative transfer model fails to accurately simulate the surface observed or if the ice is contaminated with other H_2O ice phases, with bound water in hydrated minerals, by radiation damage, or with other unanticipated absorbers with spectral features coincident with the H_2O absorptions. Europa and Enceladus exhibit strong spectral evidence for these sorts of effects.

The ice temperatures derived from our spectra are generally colder than temperatures predicted by a slow-rotator thermal model which neglects thermal inertia and segregation of bright ice from darker materials. The ice temperatures are also generally lower than temperatures derived from measurements of thermal emission, which are most sensitive to the warmest regions of a satellite's surface. Our technique is most sensitive to the coldest, brightest, ice-covered areas. Taken together, the different types of temperatures are consistent with significant thermal inertias and/or segregation of ice from darker materials, on the surfaces of satellites of all three planets. Our time-resolved experiments are also consistent with significant thermal inertias in the uppermost few millimeters of icy regions on outer Solar System satellites.

Looking toward future applications, our temperature-sensing technique could be especially powerful in disk-resolved studies, in which a much smaller range of temperatures and terrains contributes to each observed spectrum. Disk-resolved studies also open the possibility of mapping ice temperatures across the disk, and investigating the rate of diurnal heating, if regional effects of albedo, emissivity, and texture can be accurately accounted for. Alternatively, if the rate of heating can be obtained from time-resolved studies or other means, the diurnal profile can be modeled, permitting the use of this method to obtain information on albedo and emissivity effects on temperatures of different regions. Slope effects on temperature may likewise be measurable and thus may provide some topographic information. However, slope dependent patterns of albedo (and presumably composition and emissivity), such as those found on high-resolution images of Europa, may strongly dominate the temperature pattern, so very high spatial resolution observations and models may be required before these effects can be reliably disentangled.

ACKNOWLEDGMENTS

Special thanks to C. Dalla Piazza for his help at the telescope and his contribution to the development of the data reduction software, and to M. Schwartz and B. Hilbert for their assistance at the telescope in 1995 and 1998, respectively. Thanks also to B. Skiff for help selecting solar analog stars, and to G. Hansen for a timely and constructive review. W. Grundy was supported by Hubble Fellowship Grant HF-01091.01-97A awarded by the Space Telescope Science Institute, which is operated by the Association of Universities for Research in Astronomy, Inc., for NASA under Contract NAS 5-26555. Support for M. Buie was provided by NASA through Grants NAGW-5009 and NAG5-4210. J. Stansberry was supported by NASA Planetary Atmospheres Grant NAG5-4859. J. Spencer acknowledges support from NASA Grant NAG5-6794. B. Schmitt was supported by the "Programme National de Planétologie" from the French Institut des Sciences de l'Univers, CNRS. The LGGE is associated with the University Joseph Fourier, Grenoble, France.

REFERENCES

Benedix, G. K., T. L. Roush, T. C. Owen, D. P. Cruikshank, T. R. Geballe, C. M. Dalle Ore, B. N. Khare, and C. de Bergh 1998. Surface composition models of the leading surfaces of Rhea and Dione *Bull. Am. Astron. Soc.* **30**, 1101. [Abstract]

Bertie, J. E., and S. M. Jacobs 1977. Far-infrared absorption by ices I_h and I_c at 4.3 K and the power diffraction pattern of ice I_c. *J. Chem. Phys.* **67**, 2445–2448.

Bertie, J. E., and E. Whalley 1964. Infrared spectra of ices I_h and I_c in the range 4000 to 350 cm^{-1}. *J. Chem. Phys.* **40**, 1637–1645.

Brown, R. H., and D. L. Matson 1987. Thermal effects of insolation propagation into the regoliths of airless bodies. *Icarus* **72**, 84–94.

Brown, R. H., D. P. Cruikshank, and D. Morrison 1982. Diameters and albedos of satellites of Uranus. *Nature* **300**, 423–425.

Buratti, B. 1985. Application of a radiative transfer model to bright icy satellites. *Icarus* **61**, 208–217.

Buratti, B., F. Wong, and J. Mosher 1990. Surface properties and photometry of the uranian satellites. *Icarus* **84**, 203–214.

Calvin, W. M., R. N. Clark, R. H. Brown, and J. R. Spencer 1995. Spectra of the icy Galilean satellites from 0.2 to 5 μm: A compilation, new observations, and recent summary. *J. Geophys. Res.* **100**, 19,041–19,048.

Clark, R. N. 1981. Water frost and ice: The near-infrared spectral reflectance 0.65–2.5 μm. *J. Geophys. Res.* **86**, 3087–3096.

Cleveland, W. S. 1985. *The Elements of Graphing Data*. Wadsworth Advanced Books and Software, Chicago.

Cruikshank, D. P. 1980. Near infrared studies of the satellites of Saturn and Uranus. *Icarus* **41**, 246–258.

Cruikshank, D. P., and R. H. Brown 1981. The uranian satellites: Water ice on Ariel and Umbriel. *Icarus* **45**, 607–611.

Cruikshank, D. P., R. H. Brown, W. M. Calvin, T. L. Roush, and M. J. Bartholomew 1998. Ices on the satellites of Jupiter, Saturn, and Uranus. In *Solar System Ices* (B. Schmitt, C. de Bergh, and M. Festou, Eds.), pp. 579–606. Kluwer Academic, Boston.

Cruikshank, D. P., J. Veverka, and L. A. Lebofsky 1984. Satellites of Saturn: Optical properties. In *Saturn* (T. Gehrels and M. S. Matthews, Eds.), pp. 640–667. Univ. of Arizona Press, Tucson.

Dalton, J. B., and R. N. Clark 1998. Laboratory spectra of Europa candidate materials at cryogenic temperatures. *Bull. Am. Astron. Soc.* **30**, 1081. [Abstract]

DePoy, D. L., B. Atwood, P. Byard, J. Frogel, and T. O'Brien 1993. Infrared imager/spectrometer (OSIRIS). *Proc. SPIE* **1946**, 667–672.

Domingue, D. L., G. W. Lockwood, and D. T. Thompson 1995. Surface textural properties of icy satellites: A comparison between Europa and Rhea. *Icarus* **115**, 228–249.

Esposito, L. W., J. N. Cuzzi, J. B. Holberg, E. A. Marouf, G. L. Tyler, and C. C. Porco 1984. Saturn's rings: Structure, dynamics, and particle properties. In *Saturn* (T. Gehrels and M. S. Matthews, Eds.), pp. 463–545. University of Arizona Press, Tucson.

Fink, U., and H. P. Larson 1975. Temperature dependence of the water-ice spectrum between 1 and 4 microns: Application to Europa, Ganymede, and Saturn's rings. *Icarus* **24**, 411–420.

Fink, U., N. H. Dekkers, and H. P. Larson 1973. Infrared spectra of the Galilean satellites of Jupiter. *Astrophys. J.* **179**, L155–L159.

Fink, U., H. P. Larson, T. N. Gautier III, and R. R. Treffers 1976. Infrared spectra of the satellites of Saturn: Identification of water ice on Iapetus, Rhea, Dione, and Tethys. *Astrophys. J.* **207**, L63–L67.

Gafney, E. S., and D. L. Matson 1980. Water ice polymorphs and their significance on planetary surfaces. *Icarus* **44**, 511–519.

Grundy, W. M. 1995. *Methane and Nitrogen Ices on Pluto and Triton: A Combined Laboratory and Telescope Investigation.* Ph.D. thesis, University of Arizona, Tucson.

Grundy, W. M., and U. Fink 1994. Band broadening effects in bright planetary surfaces. *Bull. Am. Astron. Soc.* **26**, 1176. [Abstract]

Grundy, W. M., and B. Schmitt 1998. The temperature-dependent near-infrared absorption spectrum of hexagonal H_2O ice. *J. Geophys. Res.* **103**, 25,809–25,822.

Hanel, R., B. Conrath, F. M. Flasar, V. Kunde, W. Maguire, J. Pearl, J. Pirraglia, R. Samuelson, D. Cruikshank, D. Gautier, P. Gierasch, L. Horn, and C. Ponnamperuma 1982. Infrared observations of the saturnian system from Voyager 2. *Science* **215**, 544–548.

Hapke, B. 1981. Bidirectional reflectance spectroscopy: 1. Theory *J. Geophys. Res.* **86**, 3039–3054.

Hapke, B. 1993. *Theory of Reflectance and Emittance Spectroscopy.* Cambridge Univ. Press, New York.

Hardin, A. H., and K. B. Harvey 1973. Temperature dependences of the ice I hydrogen bond spectral shifts: I. The vitreous to cubic ice I phase transformation. *Spectrochem. Acta* **29A**, 1139–1151.

Heide, H. G. 1984. Observation on ice layers. *Ultramicroscopy* **14**, 271–278.

Helfenstein, P., J. Hillier, C. Weitz, and J. Veverka 1991. Oberon: Color photometry from Voyager and its geological implications. *Icarus* **90**, 14–29.

Horne, K. 1986. An optimal extraction algorithm for CCD spectroscopy. *Publ. Astron. Soc. Pacific* **98**, 609–617.

Jenniskens, P., D. F. Blake, and A. Kouchi 1998. Amorphous water ice. In *Solar System Ices* (B. Schmitt, C. de Bergh, and M. Festou, Eds.), pp. 139–155. Kluwer Academic, Boston.

Kargel, J. S. 1991. Brine volcanism and the interior structure of asteroids and icy satellites. *Icarus* **94**, 368–390.

Karkoschka, E. 1997. Rings and satellites of Uranus: Colorful and not so dark. *Icarus* **125**, 348–363.

Kato, M., Y. Taniguchi, S. Sawamura, and K. Suzuki 1992. Near-Infrared studies of high pressure water and ices. In *Physics and Chemistry of Ice* (N. Maeno and T. Hondoh, Eds.), pp. 83–87. Hokkaido Univ. Press, Sapporo.

Kieffer, H. H., and W. D. Smythe 1974. Frost spectra: Comparison with Jupiter's satellites. *Icarus* **21**, 506–512.

Kouchi, A., and T. Kuroda 1990. Amorphization of cubic ice by ultraviolet irradiation. *Nature* **344**, 134–135.

Kuiper, G. P., D. P. Cruikshank, and U. Fink 1970. The composition of Saturn's rings. *Sky and Telescope* **39**, 14.

Lampton, M., B. Margon, and S. Bowyer 1976. Parameter estimation in X-ray astronomy. *Astron. J.* **208**, 177–190.

Lebofsky, L. A., and J. R. Spencer 1989. Radiometry and thermal modeling of asteroids. In *Asteroids II* (R. P. Binzel, T. Gehrels, and M. S. Matthews, Eds.), pp. 128–147. Univ. of Arizona Press, Tucson.

Matson, D. L., and R. H. Brown 1989. Solid-state greenhouses and their implications for icy satellites. *Icarus* **77**, 67–81.

McCord, T. B., G. B. Hansen, F. P. Fanale, R. W. Carlson, D. L. Matson, T. V. Johnson, W. D. Smythe, J. K. Crowley, P. D. Martin, A. Ocampo, C. A. Hibbits, J. C. Granahan, and the NIMS Team 1998. Salts on Europa's surface detected by Galileo's near infrared mapping spectrometer. *Science* **280**, 1242–1245.

McCord, T. B., G. B. Hansen, D. L. Matson, T. V. Johnson, J. K. Crowley, F. P. Fanale, R. W. Carlson, W. D. Smythe, P. D. Martin, C. A. Hibbits, J. C. Granahan, and A. Ocampo 1999. Hydrated salt minerals on Europa's surface from the Galileo near-infrared mapping spectrometer (NIMS) investigation. *J. Geophys. Res.* **104**, 11,827–11,851.

Moore, J. M., E. Asphaug, D. Morrison, J. R. Spencer, C. R. Chapman, B. Bierhaus, R. J. Sullivan, F. C. Chuang, J. E. Klemaszewski, R. Greeley, K. C. Bender, P. E. Geissler, P. Helfenstein, and C. B. Pilcher 1999. Mass movement and landform degradation on the icy Galilean satellites: Results from the Galileo nominal mission. *Icarus* **140**, 294–312.

Moore, M. H., and R. L. Hudson 1992. Far-infrared spectral studies of phase changes in water ice induced by proton irradiation. *Astrophys. J.* **401**, 353–360.

Morrison, D., and D. P. Cruikshank 1973. Thermal properties of the Galilean satellites. *Icarus* **18**, 224–236.

Morrison, D., D. P. Cruikshank, and R. E. Murphey 1972. Temperatures of Titan and the Galilean satellites at 20 microns. *Astrophys. J.* **173**, L143–L146.

Morrison, D., D. P. Cruikshank, C. B. Pilcher, and G. H. Rieke 1976. Surface composition of the satellites of Saturn from infrared photometry. *Astrophys. J.* **207**, L213–L216.

Ockman, N. 1958. The infra-red and raman spectra of ice. *Adv. Phys.* **7**, 199–220.

Pilcher, C. B., C. R. Chapman, L. A. Lebofsky, and H. H. Kieffer 1970. Saturn's rings: Identification of water frost. *Science* **167**, 1372–1373.

Pilcher, C. B., S. T. Ridgway, and T. B. McCord 1972. Galilean satellites: Identification of water frost. *Science* **178**, 1087–1089.

Prockter, L. M., J. W. Head, D. A. Senske, R. T. Pappalardo, G. Neukum, R. Wagner, U. Wolf, J. Oberst, B. Giese, J. M. Moore, C. R. Chapman, P. Helfenstein, R. Greeley, H. H. Breneman, and M. J. S. Belton 1998. Dark terrain on Ganymede: Geological mapping and interpretation of Galileo Regio at high resolution. *Icarus* **135**, 317–344.

Roush, T. L., D. P. Cruikshank, T. C. Owen, T. R. Geballe, G. K. Bendix, C. de Bergh, K. S. Noll, and B. N. Khare 1998a. Titania and Oberon: Surface composition from new near-infrared observations and reflectance models. *Bull. Am. Astron. Soc.* **30**, 1100. [Abstract]

Roush, T. L., T. Geballe, D. P. Cruikshank, T. Owen, G. Bendix, and C. M. Dalle Ore 1998b. Water ice on Titania and Oberon: New high resolution near-infrared (1.4–2.52 μm) spectra. *Proc. Lunar Planet. Sci. Conf. 29th*, 1632. [Abstract]

Schmitt, B., E. Quirico, F. Trotta, and W. M. Grundy 1998. Optical properties of ices from UV to infrared. In *Solar System Ices* (B. Schmitt, C. de Bergh, and M. Festou, Eds.), pp. 199–240. Kluwer Academic, Boston.

Soifer, B. T., G. Neugebauer, and K. Matthews 1981. Near-infrared spectrophotometry of the satellites and rings of Uranus. *Icarus* **45**, 612–617.

Spencer, J. R. 1987a. *The Surfaces of Europa, Ganymede, and Callisto: An Investigation Using Voyager IRIS Thermal Infrared Spectra.* Ph.D. thesis, University of Arizona, Tucson.

Spencer, J. R. 1987b. Thermal segregation of water ice on the Galilean satellites. *Icarus* **69**, 297–313.

Spencer, J. R., L. A. Lebofsky, and M. V. Sykes 1989. Systematic biases in radiometric diameter determinations. *Icarus* **78**, 337–354.

Strazzulla, G., G. Leto, G. A. Baratta, and F. Spinella 1991. Ion irradiation experiments relevant to cometary physics. *J. Geophys. Res.* **96**, 17,547–17,552.

Sykes, M. V., R. M. Cutri, L. A. Lebofsky, and R. P. Binzel 1987. IRAS serendipitous survey observations of Pluto and Charon. *Science* **237**, 1336–1340.

Taylor, M. J., and E. Whalley 1964. Raman spectra of ices I_h, I_c, II, III, and V. *J. Chem. Phys.* **40**, 1660–1664.

Urquhart, M. L., and B. M. Jakosky 1996. Constraints on the solid-state greenhouse effect on the icy Galilean satellites. *J. Geophys. Res.* **101**, 21,169–21,176.

Verbiscer, A., and P. Helfenstein 1998. Reflectance spectroscopy of icy surfaces. In *Solar System Ices* (B. Schmitt, C. de Bergh, and M. Festou, Eds.), pp. 157–197. Kluwer Academic, Boston.